Sunrise Chromospheric Infrared spectroPolarimeter (SCIP) for SUNRISE III: optical design and performance

Tsuzuki, Toshihiro, Katsukawa, Yukio, Uraguchi, Fumihiro, Hara, Hirohisa, Kubo, Masahito, et al.

SPIE.

Sunrise Chromospheric Infrared spectroPolarimeter (SCIP) for Sunrise III: Optical Design and Performance

Toshihiro Tsuzuki[a], Yukio Katsukawa[a], Fumihiro Uraguchi[a], Hirohisa Hara[a], Masahito Kubo[a], Yoshifumi Nodomi[a], Yoshinori Suematsu[a], Yusuke Kawabata[a], Toshifumi Shimizu[b], Achim Gandorfer[c], Alex Feller[c], Bianca Grauf[c], Sami Solanki[c,e], and Jose Carlos del Toro Iniesta[d]

[a]National Astronomical Observatory of Japan, 2-21-1 Osawa, Mitaka, Tokyo 181-8588, Japan
[b]Institute of Space and Astronautical Science, Japan Aerospace Exploration Agency, 3-1-1 Yoshinodai, Chuo-ku, Sagamihara, Kanagawa 252-5210, Japan
[c]Max-Planck-Institut für Sonnensystemforschung, Justus-von-Liebig-Weg 3, 37077 Göttingen, Germany
[d]Instituto de Astrofísica de Andalucía, Glorieta de la Astronomía, s/n 18008 Granada, Spain
[e]School of Space Research, Kyung Hee University, Yongin, Gyeonggi-Do, 446-701, Republic of Korea

ABSTRACT

The Sunrise Chromospheric Infrared spectroPolarimeter (SCIP) is a near-IR spectro-polarimeter instrument newly designed for Sunrise III, which is a balloon-borne solar observatory equipped with a 1 m optical telescope. To acquire high-quality 3D magnetic and velocity fields, SCIP selects the two wavelength bands centered at 850 nm and 770 nm, which contain many spectrum lines that are highly sensitive to magnetic fields permeating the photosphere and chromosphere. To achieve high spatial and spectral resolution (0.21 arcsec and 2×10^5), SCIP optics adopt a quasi-Littrow configuration based on an echelle grating and two high-order aspheric mirrors. Using different diffraction orders of the echelle grating, dichroic beam splitter, and polarizing beam-splitters, SCIP can obtain s- and p-polarization signals in the two wavelength bands simultaneously within a relatively small space. We established the wavefront error budget based on tolerance analysis, surface figure errors, alignment errors, and environmental changes. In addition, we performed stray light analysis, and designed light traps and baffles needed to suppress unwanted reflections and diffraction by the grating. In this paper, we present the details of this optical system and its performance.

Keywords: Sunrise III, balloon-borne solar observatory, SCIP, Spectro-polarimeter, Ca ii lines, K i lines

1. INTRODUCTION

The Sunrise[1] balloon-borne solar observatory comprises a 1-meter aperture optical solar telescope and multiple focal plane instruments. Sunrise is capable of continuous observation at an altitude of 35 km for 24 hours a day, for five days or more. This makes it possible to perform not only ultraviolet observations in the 200–300 nm wavelength range, which is impossible on the ground, but also stable visible and infrared observations without the influence of atmospheric turbulence. In the past two Sunrise flight experiments, the photosphere was imaged only in visible and ultraviolet light of wavelengths shorter than 550 nm. However, visible and near-infrared polarization spectrometers with high sensitivity to the Zeeman effect are required to measure the dynamics between the photosphere and the chromosphere and its magnetic field. Therefore, a new near-infrared polarization spectrometer called Sunrise Chromospheric Infrared spectro-Polarimeter[2,3](SCIP), is under development for the third Sunrise flight experiment (Sunrise III) to perform high-resolution and high-sensitivity polarization observations of the photosphere and chromosphere. If the Sunrise balloon experiment is equipped with a near-infrared polarization spectrograph, it can achieve 0.2 arcsecond angular resolution (better than that of

---

the Hinode visible light telescope[4]), and 0.03 % polarization sensitivity (1σ, thrice that of Hinode) at a time resolution of 10 s. Furthermore, by observing a large number of spectral lines simultaneously, it is possible to obtain a three-dimensional magnetic field and velocity structure that can continuously cover the photosphere and chromosphere. For example, the Ca II lines (849.8 nm, 854.2 nm) are spectral lines emitted from the middle of the chromosphere (plasma β <1), and there are several Fe I lines in its vicinity that can be used to observe the photosphere. Particularly, the Fe I line (846.8 nm) is a spectral line with high sensitivity to the Zeeman effect.[5] In addition, the observation of the K I lines (766.4 nm, 769.9 nm) enables measuring the magnetic field of the lowest temperature layer at the boundary between the photosphere and chromosphere.[6] In this study, SCIP selects the two wavelength bands centered at 850 nm and 770 nm as the target wavelength.

Spectro-polarimetric observations of the Sun have been performed both with ground-based telescope instruments (e.g., Visible Spectro-Polarimeter[7](ViSP) in DKIST[8]) and with space telescope instruments (e.g., Hinode Spectro-Polarimeter[9] in Hinode space telescope[4]). Spectro-polarimeters for ground-based telescopes have the advantage of covering a wide range of wavelengths. However, this requires a sufficiently large space to separate the dispersed light. For example, ViSP covers an extremely wide wavelength range (380–1600 nm) and the optics of ViSP, which is an echelle spectrograph using one OAP as collimator and lenses as camera, is relatively large size that is fit in the 16 m diameter rotating coudé room. On the other hand, spectro-polarimeter for space telescope has the advantages of sufficient integration time and the ability to avoid atmospheric absorption of wavelengths. However, due to the limited space available for the instrument, the spectral coverage is narrow. For example, the optics of Hinode Spectro-Polarimeter which is an off-axis Littrow-Echelle spectrograph was realized within a relatively small space. However, its spectral coverage was also narrow with a maximum of 4.77Å. SCIP is mounted on a balloon-borne telescope, so the space available for the optics is limited. Thus, the challenge of optical design of SCIP optics is to achieve high spatial and spectral resolution, and simultaneous imaging of two wavelength bands and polarizations within the limited space of the balloon gondola. In this study, we describe the optics of SCIP and evaluate the performance.

2. FORE-OPTICS AND SCIP SPECIFICATIONS

The SUNRISE telescope is a Gregorian-style telescope with a maximum aperture of 1-meter.[10] The light collected by the telescope is distributed to SCIP by Image Stabilization and Light Distribution[10](ISLiD), in addition to image stabilization by the tip-tilt mirror controlled by the Correlating wavefront sensor[11](CWS). For SCIP, the front optics is the telescope+ISLiD, and the interface between SCIP and ISLiD is the focus of the telescope relayed by ISLiD. Information about the incident light from ISLiD to SCIP is described in Tab. 1 and the overall wavefront error (WFE) budget to obtain nearly diffraction-limited resolution images at the SCIP observing wavelength is also described in Tab. 2.

Table 1: Information about the incident light from ISLiD to SCIP

Items	Specifications
Effective focal length	24237 mm (F/24.24)
Plate scale	0.0936 ″/11 μm
Field-of-view (FOV)	6.8 × 6.8 mm (at the SCIP slit)
Exit pupil position	5.59 m (from the interface focus position generated by ISLiD)

The scientific requirements and the requirement specifications for the SCIP optics are summarized in Tab. 3. SCIP optics are required to achieve high spatial and spectral resolutions, simultaneous imaging of two wavelength bands and two polarizations within the limited space of the balloon gondola.

3. OPTICAL DESIGN POLICY

Based on the design specifications described in the previous section, the optical design policy for the spectrograph (SP) and slit-jaw optics (SJ) is described below.

Table 2: Overall wavefront error budget

Items	WFE (nm RMS)	Strehl ratio at 850 nm	Note
Telescope+ISLiD	60.0	0.823	$\lambda/5$ at 300 nm in Sunrise I (in Ref 12).
Relative defocus	15.4	0.987	0.25 mm relative defocus, including 0.1 mm as alignment and 0.15 mm as in-flight change
Attitude jitter	30.1	0.95	Corresponding to $0.077''(3\sigma)$, including (1) $0.06''(3\sigma)$ achievements in Sunrise II, (2) $0.035''(3\sigma)$ corresponding to $1''(3\sigma)$ tilt stability of the scan mirror, (3) $\phi 0.034''$ corresponding to 4 μm due to PMU wobbling
SCIP	48.0	0.883	Detailed allocation is described in Fig. 7b
Total (RSS)	83.9	0.683	

Table 3: Requirement based specifications for SCIP optics.

Items	Scientific requirements	Requirement specifications for the SCIP optics
Wavelength	Combination of spectral lines that allows seamless and simultaneous observation of the photosphere and chromosphere	(1) 846.6–854.9 nm (in air) including Ca I lines, (2) 765.5–771.6 nm (in air) including K I lines
FOV	Large enough to study dynamic phenomena (i.e., sufficient coverage of supergranulation)	58 arcsecond (slit length) $\times$ 58 arcsecond (by scanning)
Spatial resolution	To achieve a diffraction-limited resolution of 0.21 arcseconds at 850 nm for the entire optical system including the telescope.	The wavefront error of SCIP spectrograph alone must be less than 48 nm RMS.
Spectral resolution	Sufficient wavelength resolution for magnetic field observation in the chromosphere	$\lambda/\Delta\lambda = 2 \times 10^5$ at 846.6 nm. λ and $\Delta\lambda$ indicates wavelength and wavelength sampling, respectively.
Polarization	High-precision observation of linear and circular polarization	Simultaneous observation of two linearly polarized components that are orthogonal to each other
Throughput	To observe as many photons as possible.	Diffracted light from the slit must be used up to F/11 (See Fig. 3)
Slit monitor	To acquire diffraction-limited solar images at the slit for the telescope's orientation adjustment.	The slit-jaw optics whose observation wavelength is continuous light of 770.5 $\pm$ 0.5 nm should be able to monitor the slit. The wavefront error of its slit-jaw optics should be less than 34 nm RMS.
Packaging	Allocation of SCIP in the balloon gondola.	The overall SCIP optics must fit within the allocated area (L 940 mm $\times$ W 500 mm $\times$ H 340 mm)

(1) All-reflecting spectrometer

To achieve high spectral resolution, a plane echelle grating spectrometer with zero grating aberration has an advantage over a concave grating spectrometer in minimizing aberrations. Echelle gratings are generally used as a reflective grating in high order at large angle of incidence and desirable to be used in Littrow configuration to achieve the highest grating efficiency. However, the strict Littrow configuration is not practical because incident and diffracted beams overlap. To avoid the problem, there are two design choices of angle of the incident chief ray relative to the echelle: (1) in-plane design, and (2) off-plane design. We use an in-plane design that prevents the slit image from being tilted at the image plane, in

order to maximize the effective use of the detector area. For practical in-plane designs which collimator and camera optics are separated, the angle of incidence at the grating is not the same as the blaze angle to ensure clearance between the collimator and camera optics. This leads to a decrease in diffraction efficiency because the diffraction efficiency decreases as the absolute value of the angle difference between the angle of incidence and the angle of blaze to the grating increases. Therefore, the angle of incidence to the grating should be close to the blaze angle (i.e., quasi-Littrow configuration), with sufficient clearance between the collimator and camera mirrors. For collimators and camera optics, all-reflecting optics using mirrors (for example, Czerny-Turner mounting[13]) are more advantageous in terms of the number of elements rather than lens optics, which require a large number of elements to suppress chromatic aberration.

(2) High spectral resolution
To achieve high spectral resolution, the spectrograph uses higher diffraction orders of an echelle grating. We selected a commercial echelle grating from Richardson Gratings™, which is characterized by the Richardson catalogue code 53999ZD06–121E. As its groove density is 110/mm, the diffraction angle at 850 nm is the same as that at 770 nm, so that the camera mirror can be shared between the two wavelength bands.

(3) Simultaneous observation of the two wavelength bands
In order to achieve simultaneous observation of two wavelength bands, a dichroic beam splitter (long pass filter) tilted toward the optical axis is placed behind the camera mirror to divide the two wavelength bands into two channels. In addition, a narrow-band filter is placed in each channel after the beam splitter to extract the observed wavelength region.

(4) High spatial resolution
Owing to the use of planar gratings, the collimator and camera mirrors are the major contributors to the aberration in SCIP. In the Czerny-Turner mounting in quasi-Littrow configuration, the angles between the normal direction of these mirrors and the incident chief rays contribute to the aberrations. Therefore, it is necessary to make the bend angle of the collimator and camera mirrors to be as small as possible without interference between the optical elements to reduce the aberration. The shape of the collimator and camera mirrors is determined by optimization with higher-order components to minimize wavefront aberrations. Since the dichroic beam splitter tilted to the optical axis is placed in the converging light, there is a difference in aberration between the transmitted 850 nm channel and the reflected 770 nm channel. This aberration difference is eliminated without increasing the number of elements, by wedging the rear surface of the dichroic beam splitter. In addition, it is desirable to minimize the number of optical elements to minimize the effect of surface figure errors and installation errors on the optical elements.

(5) Simultaneous observation of two polarizations
By placing a polarization beam splitter (PBS) before each detector, two orthogonal linearly polarized components are spatially separated and imaged on each single detector (Fig. 1).

(6) Slit-jaw optics
Since the observation wavelength of the slit-jaw optics is as narrow as 770.5 ± 0.5 nm and the chromatic aberration is negligible, the slit-jaw optics is designed with lenses. However, since the wavelength region from ISLiD is a continuous spectrum longer than 700 nm, it is necessary to treat the unwanted wavelength light properly to suppress stray light to the SP optics and SJ detector. Therefore, a notch filter and a narrow-band filter are placed just before the lenses to limit the wavelength band. The unwanted light transmitted by the notch filter has most of the energy of the incident light. In order to suppress this unwanted light from entering the SP optics and SJ lenses, a black baffle is placed after the filter such that the unwanted light hits it several times and is damped to an acceptable level.

4. SCIP-SP OPTICAL SYSTEM

The SCIP optics comprise SP and SJ. In this section, the design and optical performance of SCIP-SP are described.
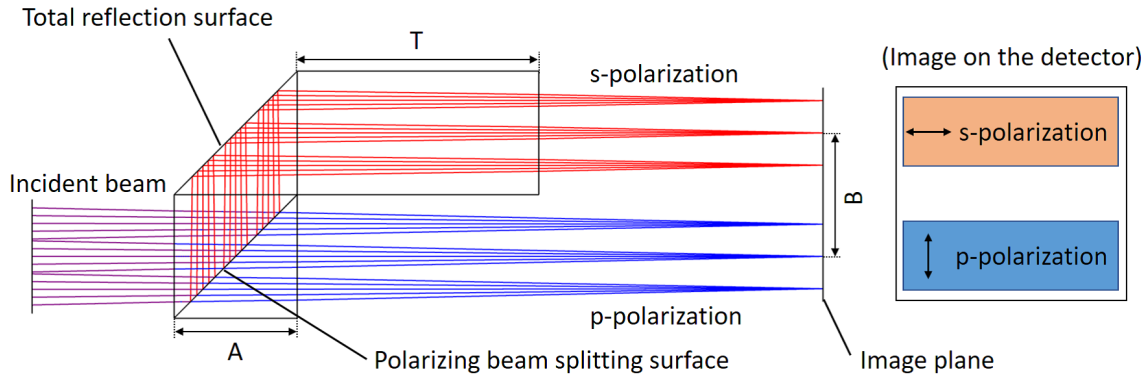
Figure 1: Geometry and optical path of the PBS, using a cube beam splitter with a dielectric coating at the 45° surface, and with AR coatings on the entrance and exit surfaces. To adjust the focus position, a glass block is inserted in the optical path of the s-polarization that is reflected at the 45° surface. The thickness of the glass block (T) is adjusted according to the refractive index and wavelength. A: edge length of cube beam splitter, B: beam separation length, T: thickness of focus adjustment block
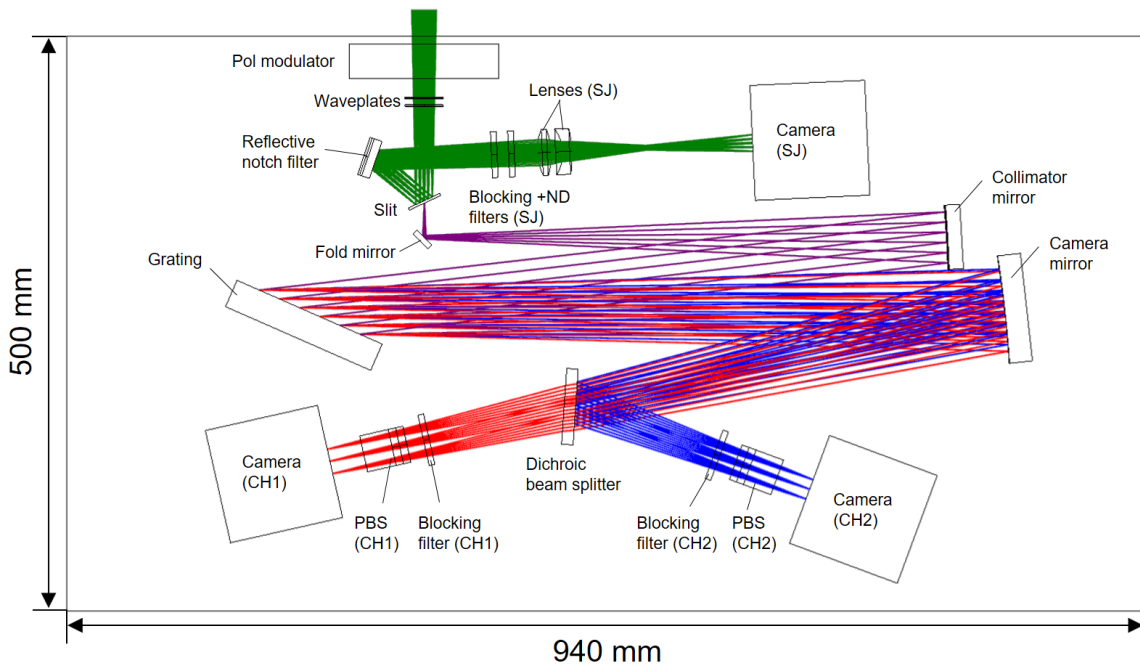

Figure 2: 3D layout and optical path diagram of SCIP. The colored rays represent the following: (red) SP CH1, (blue) SP CH2, (green) SJ.

4.1 SCIP-SP design performance

The SCIP-SP optical layout is shown in Fig. 2. The incident convergent light from the ISLiD (F/24.2) first passes through the two rotating waveplates and enters the slit. SCIP-SP uses light that has passed through the slit. The light transmitted through the slit is spread out at (F/24.2) in the slit length direction (i.e., spatial direction), and it spreads more in the slit width direction (i.e., dispersion direction) by diffraction. Since the observing wavelength is in the near-infrared wavelength range, we need to take into account the effect of diffraction by a slit 11 μm in width in the vertical direction to the slit. As shown in Fig. 3, the energy contained in the F/11 beam size are 85 % at both 850 nm and 770 nm. Thus, in optical design, we use the F/11 beam in the direction

vertical to the slit, while the F/24.2 beam is used in the direction parallel to the slit. The SCIP-SP main optics is
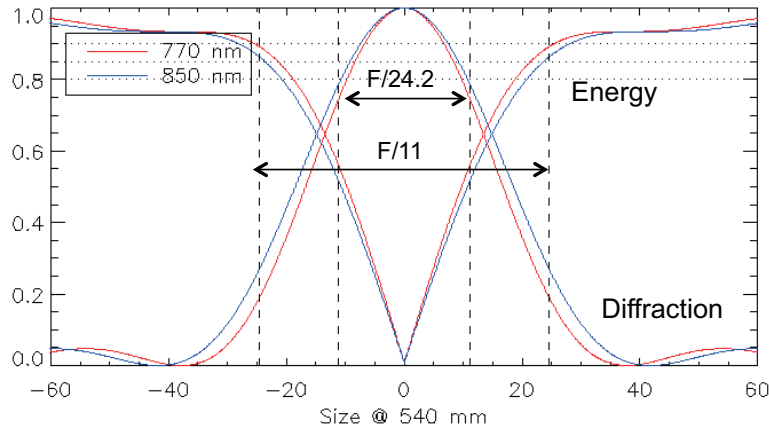

Figure 3: Slit diffraction pattern at the collimator mirror when the mirror is located at 540 mm from the slit.

the modified Czerny-Turner mounting[13] comprising an echelle grating and two mirrors (a collimator mirror and a camera mirror) in a quasi-Littrow configuration. The light from the slit is collimated by the collimator mirror and enters the grating. The collimated light is diffracted by the echelle grating with groove density 110/mm, so that the two wavelength bands are observed simultaneously using different diffraction orders: the 19th order to observe the 850 nm wavelength band (CH1), and the 21st order to observe the 770 nm wavelength band (CH2). The grating has a blaze angle of 64°, but the angle of incidence to the grating was designed to be 59.6° to maintain the clearance between the collimator mirror and the camera mirror. The diffracted parallel light from the echelle grating becomes a converging light after passing through the camera mirror. The two channels are separated using a dichroic beam splitter with a long-pass filter coating. In each channel, the required wavelength bands are extracted through a blocking filter. Polarization measurement is performed using a rotating waveplate and a PBS for each channel. In order to achieve high imaging performance, the mirror surface forms of the collimator and camera mirrors were determined by optimization. These surface forms are similar to off-axis parabolas as in the usual Littrow configuration, however, higher aspheric terms are found to be needed to sufficiently suppress the aberration. Therefore, we changed the surface type from the off-axis parabola to on-axis spherical surface to add higher order aspheric terms. The final forms are obtained from the sum of the spherical and the polynomial aspheric terms, which is expressed as the following equation on a local coordinate (x, y):

$$z(x,y) = \frac{cr^2}{1 + \sqrt{1 - (1+k)c^2r^2}} + \sum_{i=0}^{5}\sum_{j=0}^{5} C_{ij}x^i y^j \,, \tag{1}$$

where c is the curvature, r is the radial distance from the center, k is a conic constant, and x and y are local coordinates normalized by the normalization radius. The polynomial coefficients (C_{ij}) of these mirrors are given in Tab. 4. Furthermore, to eliminate the aberration difference caused by the difference between the transmitted and reflected ray paths in the two channels, the beam splitter is designed as a wedged plate instead of a plane-parallel plate. All these optics are within the SCIP allocated area (L 940 mm × W 500 mm × H 340 mm, black rectangle area in Fig. 2). The basic optical parameters of SCIP-SP are summarized in Tab. 5. By optimizing the surface parameters of the collimator and camera mirrors as well as the positions/tilts of the mirrors and the wedge of the dichroic beam splitter, we realized an efficient design with a small wavefront error in the wavefront error budget. Fig. 4 and Fig. 5 show spot diagrams and the RMS wavefront error plotted against the wavelength for the two channels, respectively. Fig. 4 indicates that the spot size is sufficiently small with respect to the airy disk at both ends and the center of the slit, and at both ends and at the center of the wavelength band. Fig. 5 indicates that the wavefront errors within each wavelength range of each channel are less than 0.006 λ in both the center and edge positions of the slit. The worst wavefront error of the two channels is 4.6 nm RMS.

Table 4: Surface parameters of the collimator and camera mirrors. Surface forms of these mirrors are expressed by Equation (1) on the local coordinate normalized by the normalization radius. The odd orders of x were set to be zero so that these surfaces are symmetrical to the x-axis.

Parameter	Unit	Collimator mirror	Camera mirror
c	1/mm	-0.000942867	-0.000942665
k		0	0
Normalization radius	mm	50	50
C_{10}	mm	0	0
C_{01}	mm	0	0
C_{20}	mm	0	0
C_{11}	mm	0	0
C_{02}	mm	0.009647008	0.020388942
C_{30}	mm	0.010968332	-0.01581678
C_{21}	mm	0	0
C_{12}	mm	0.013476503	-0.014150569
C_{03}	mm	0	0
C_{40}	mm	0.002231871	-0.001831818
C_{31}	mm	0	0
C_{22}	mm	0.001922144	-0.001356516
C_{13}	mm	0	0
C_{04}	mm	0.000710579	0.00010658
C_{50}	mm	0.000105187	-0.000251339
C_{41}	mm	0	0
C_{32}	mm	0.000383567	-0.000163616
C_{23}	mm	0	0
C_{14}	mm	0.000079695	-0.000194229
C_{05}	mm	0	0

4.2 SCIP-SP Tolerance analysis and error budget plan

We conducted tolerance analyses to evaluate the performance, including assembly and manufacturing errors and determined the number and stoke of the compensators. Based on the sensitivity and Monte Carlo analysis results with the initial feasible tolerance set, we determined the required compensators and alignment plan on each local coordinate system as follows:

(1) adjust the x- and y-tilt of the fold mirror to align the optical axis of incident light and that of SP,

(2) adjust the z-shift of the collimator mirror to compensate for the manufacturing error of the radius of curvature of the collimator mirror and to make the incident light to the grating parallel,

(3) adjust the z-tilt of the grating to compensate for the tilt of the dispersion direction,

(4) adjust x-and y-tilts of the camera mirror, the y-tilt of the grating, and the defocus of the detector to compensate for the image quality,

(5) adjust the x- and y-shifts of the detector to compensate for the shift of the image position,

(6) adjust the x- and y-shifts of the blocking filter and the PBS to avoid the vignetting of optical elements.

We revised the tolerance values to more feasible values and performed a Monte Carlo analysis under this alignment plan. The tolerance table of SP are shown in Fig. 6a and the results of a Monte Carlo analysis assuming parabolic tolerance distributions (N = 1000) are shown in Fig. 7a. The RMS wavefront error at cumulative probability (3σ) is 6.6 nm RMS, which indicates that the wavefront error degradation due to installation and manufacturing error is 4.7 nm RMS by subtraction using root sum squares (RSS) approach. The error budget plan for imaging performance is also shown in Fig. 7b. Here, we assume that the surface figure errors, transmitted wavefront

Table 5: SCIP basic optical parameters.

Spectropolarimeter (SP)

Spectrograph Type		Modified Czerny-Turner mounting in quasi-Littrow configuration
Wavelength range		(CH1): 846.830–854.930 nm (in vacuum)
		(CH2): 765.708–771.808 nm (in vacuum)
Plate scale (spatial)		0.0935″/pixel
Plate scale (dispersion)		(CH1): 42.3 mÅ/pixel at 846.6 nm (equivalent to R=200000)
		(CH2): 38.5 mÅ/pixel at 765.5 nm
Waveplate#1	Shape & material	Plane parallel plate (t=1.43 mm), quartz
Waveplate#2	Shape & material	Plane parallel plate (t=1.64 mm), sapphire
Slit	Shape & material	Plane parallel plate (t=2 mm), fused silica
	Slit width & length	11 μm × 6.8 mm (0.0936″ × 58″)
	Tilt angle	25° to the incident optical axis from ISLiD
Fold mirror	Mirror surface shape	Planer
Collimator mirror	Mirror surface shape	Spherical plus XY polynomial
	Curvature radius	R=1060.595 mm
Grating	Grating type	Planar constant-line-space grating
	Groove spacing & blaze angle	110/mm & 64°
	Catalogue code	53999ZD06–121E in Richardson catalogue
	Diffraction order	(CH1):19th, (CH2):21st
	Angle of incidence	59.6° relative to the grating surface normal
Camera mirror	Mirror surface shape	Spherical plus XY polynomial
	Curvature radius.	R=1060.822 mm
Dichroic beam splitter	Shape & material	Wedged plate (t=10 mm), fused silica
	Wedge angle	0.176° relative to the front surface
Blocking filters	Shape & material	Plane parallel plate (t=5 mm), fused silica
PBSs	Shape	Comprising a right angle prism, a rhomboid prism, and a rectangular cuboid (Fig. 1)
	Material	BSL7Y
	Dimensions (A, B, T)	(CH1): (13 mm, 13 mm, 25.489 mm)
		(CH2): (13 mm, 13 mm, 25.409 mm)
Camera sensor	Sensor type	Back-illuminated CMOS
	Pixel array & pixel size	2048 (H) × 2048 (V), 11 μm × 11 μm

Slit-jaw (SJ)

Imaging optics		Doublet (air-spaced two lenses)
FOV		7.6 mm × 7.6 mm (equivalent to 64″ × 64″)
Wavelength band		770.208–771.208 nm (in vacuum)
Plate scale		0.0936″/pixel
Magnification		1.0
Reflective notch filter	Shape & material	Wedged plate (t=9 mm), CLEARCERAM
	Wedge angle	9.0° relative to the front surface
Blocking filter	Shape & material	Plane parallel plate (t=5 mm), BK7
ND filter	Shape & material	Plane parallel plate (t=5 mm), BK7
SJ-Lens#1	Shape & material	Bi-convex spherical lens (t=12 mm), BSL7Y
	Curvature radii of two surfaces	R1=48.646 mm & R2=62.758 mm
SJ-Lens#2	Shape & material	Meniscus spherical lens (t=8 mm), BSL7Y
	Curvature radii of two surfaces	R1=36.294 mm & R2=112.642 mm
Camera sensor	Specifications	Same as SP

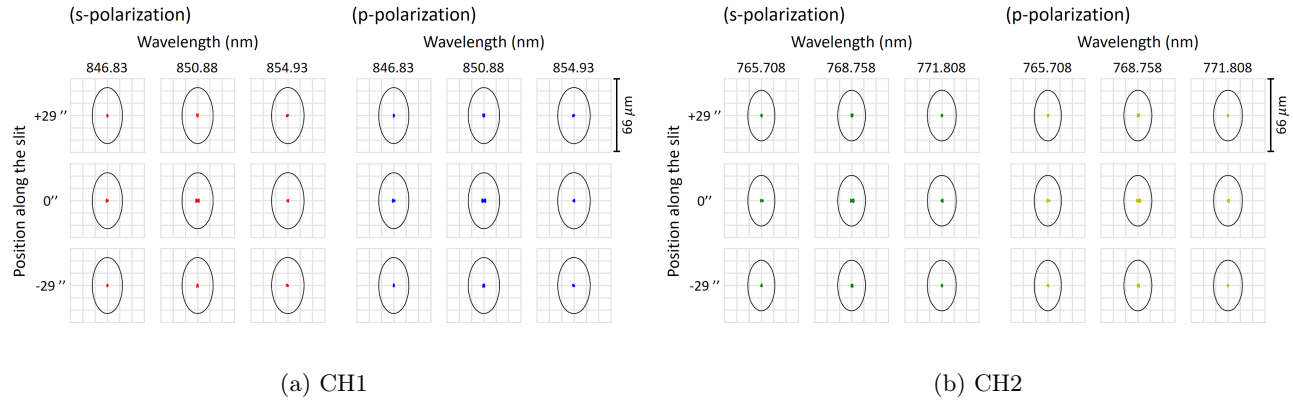(a) CH1   (b) CH2

Figure 4: Spot diagrams of SCIP-SP optical system for the two channels. (a) CH1 (left for s-pol, right for p-pol), (b) CH2 (left for s-pol, right for p-pol). The horizontal direction indicates dispersion direction which shows the performance at both ends and the center of the wavelength band. The vertical direction indicates the spatial direction which shows the performance at both ends and the center of the slit. The black ellipse in the center represents an airy disk where F/11 in the wavelength direction and F/24.2 in the spatial direction. The size of the box is 66 μm (equivalent to 6 pixels), which corresponds to a 0.56 arcsec in space, and a wavelength of 0.2538Å (CH1), 0.231 Å (CH2), respectively.

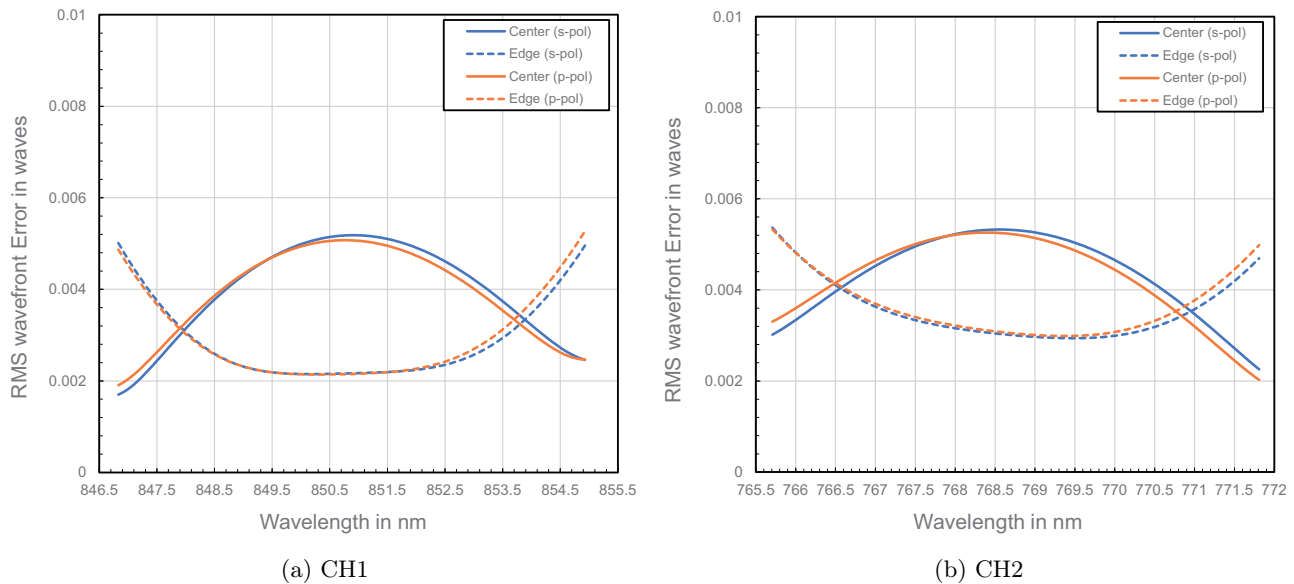(a) CH1   (b) CH2

Figure 5: RMS wavefront error plotted against the wavelength of SCIP-SP optical system. The horizontal axis indicates wavelength, and vertical axis indicates RMS wavefront error in the waves.

errors, and the adjustment errors are set to feasible values. The total RSS value is 48.0 nm RMS, which satisfies the requirements (48 nm RMS). The results of the error assessment due to environmental changes (temperature, humidity, and gravity direction) are reported in Ref. 14

5. SCIP-SJ OPTICAL SYSTEM

This section describes the design and optical performance of the SJ optics.

Element	Shift/Tilt	Unit	Tolerance	
			Manufacturing error	Installation error
SLIT	Shift (X/Y/Z)	mm	0.1/0.1/0.1	0.1/0.1/0.1
	Tilt (X/Y/Z)	arcmin.	1/1/1	1/4/10
Fold mirror	Shift (X/Y/Z)	mm	0.1/0.1/0.1	0.5/0.5/0.1
	Tilt (X/Y/Z)	arcmin.	1/1/2	1/1/18
Collimator mirror	Shift (X/Y/Z)	mm	0.1/0.1/0.1	0.1/0.1/0.1
	Tilt (X/Y/Z)	arcmin.	1/1/2	1/1/6
Grating	Shift (X/Y/Z)	mm	0.1/0.1/0.5	0.5/0.5/0.5
	Tilt (X/Y/Z)	arcmin.	1/1/9	1/1/2.5
Camera mirror	Shift (X/Y/Z)	mm	0.1/0.1/0.1	0.1/0.1/0.1
	Tilt (X/Y/Z)	arcmin.	1/1/2	1/1/3
Dichroic beam splitter	Shift (X/Y/Z)	mm	0.1/0.1/0.1	0.5/0.5/0.5
	Tilt (X/Y/Z)	arcmin.	1/1/1	1/4/6
Blocking filter (CH1 & CH2)	Shift (X/Y/Z)	mm	0.1/0.1/0.1	0.5/0.5/0.5
	Tilt (X/Y/Z)	arcmin.	2/2/2	18/18/18
PBS (CH1 & CH2)	Shift (X/Y/Z)	mm	0.1/0.1/0.1	0.5/0.5/0.5
	Tilt (X/Y/Z)	arcmin.	2/2/2	5/5/5
Camera sensor (CH1 & CH2)	Shift (X/Y/Z)	mm	0.1/0.1/0.1	0.1/0.1/0.1
	Tilt (X/Y/Z)	arcmin.	1/1/2	1/1/18

(a) Tolerance table (SP)

Element	Shift/Tilt	Unit	Tolerance	
			Manufacturing error	Installation error
Reflective notch filter	Shift (X/Y/Z)	mm	0.1/0.1/0.1	0.5/0.5/0.1
	Tilt (X/Y/Z)	arcmin.	1/1/2	1/4/18
Blocking filter (SJ)	Shift (X/Y/Z)	mm	0.1/0.1/0.1	0.5/0.5/0.5
	Tilt (X/Y/Z)	arcmin.	2/2/2	18/18/18
ND filter	Shift (X/Y/Z)	mm	0.1/0.1/0.1	0.5/0.5/0.5
	Tilt (X/Y/Z)	arcmin.	2/2/2	18/18/18
SJ-Lens #1	Radius of curvature	mm	0.020(front), 0.033(rear)	-
	Thickness	mm	0.05	-
	Shift (X/Y/Z)	mm	0.05/0.05/0.05	0.02/0.02/0.05
	Tilt (X/Y/Z)	arcmin.	1/1/-	2/2/-
SJ-Lens #2	Radius of curvature	mm	0.017(front), 0.167(rear)	-
	Thickness	mm	0.05	-
	Shift (X/Y/Z)	mm	0.05/0.05/0.05	0.02/0.02/0.05
	Tilt (X/Y/Z)	arcmin.	1/1/-	2/2/-
Unit of two lenses	Shift (X/Y/Z)	mm	-	0.05/0.05/0.05
	Tilt (X/Y/Z)	arcmin.	-	12/12/-
Camera sensor (SJ)	Shift (X/Y/Z)	mm	0.1/0.1/0.1	0.1/0.1/0.1
	Tilt (X/Y/Z)	arcmin.	1/1/2	1/1/18

(b) Tolerance table (SJ)

Figure 6: Tolerance tables of SP and SJ
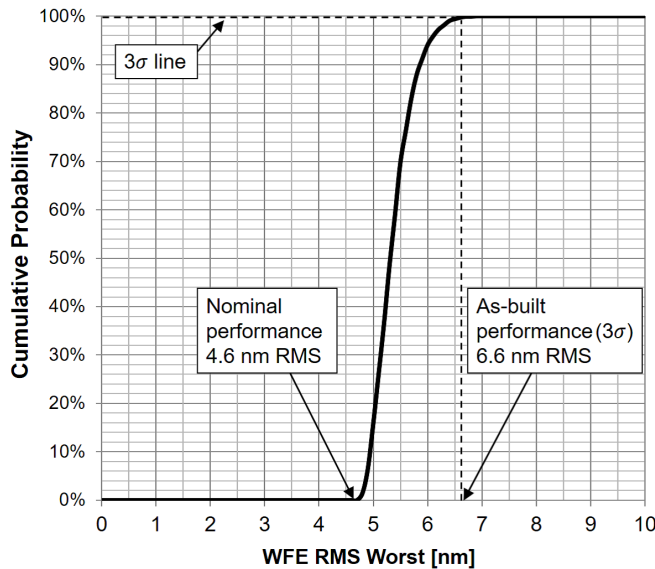
(a) Monte Carlo analysis result (SP)

Error factor		RMS wavefront error [nm]
Nominal performance		4.6
Surface figure error	due to manufacturing	37.7
	due to mounting	18.7
Installation error (3σ) including manufacturing error		4.7
Adjustment error of compensators		14.9
Focus position difference between s-pol and p-pol by PBS manufacturing error		6.4
Environmental change (temperature, humidity and gravity direction)		15.0
Root sum square		48.0

(b) RMS wavefront error budget plan (SP)

Figure 7: Monte Carlo analysis results and an error budget plan for RMS wavefront error. (a) Monte Carlo analysis result. The Monte Carlo simulation is performed with 1,000 trials. We assumed a parabolic distribution, and an adjustment using nine compensators. (b) RMS wavefront error budget plan.

5.1 SCIP-SJ design performance

The function of SCIP-SJ optics is to observe a 2D image around the slit. The SCIP-SJ optical layout is shown in Fig. 2. SCIP-SJ uses light reflected by the slit, which first enters the reflective notch filter. The reflective notch filter has a notch filter coating on the front side, which reflects the wavelength of 770.5 ± 60 nm (FWHM) and transmits unwanted wavelengths. The unwanted light transmitted by the reflective notch coating which has large energy compared to the reflected light, is reflected and attenuated several times in a black baffle located after the reflective notch filter. In addition, the rear surface of the reflective notch filter is shaped as a wedge, so that the height of the optical axis of both transmitted and reflected lights at the rear surface do not match that of reflected light at the front surface. The light reflected from the reflective notch filter is then passed through a blocking filter (SJ) to extract only the required wavelength band of 770.708 ± 0.5 nm. The light passing through the ND filter then enters the doublet lens, which forms an 1x image of the slit on the detector surface. Since SJ

has a sufficiently narrow wavelength band, the doublet lens was able to achieve sufficient imaging performance with the same glass, instead of multiple glass materials required for chromatic aberration correction. We selected the lens material as BSL7Y (OHARA Inc.) for a low refractive-index homogeneity. The basic optical parameters of SCIP-SJ are also summarized in Tab. 5.

Fig. 8 shows spot diagrams and RMS wavefront errors in the SCIP-SJ FOV. Fig. 8a indicates that at all positions in the field of view, the spot size is small enough for the airy disc. Fig. 8b indicates that the worst RMS wavefront error in the SCIP-SJ FOV is 3.5 nm RMS.

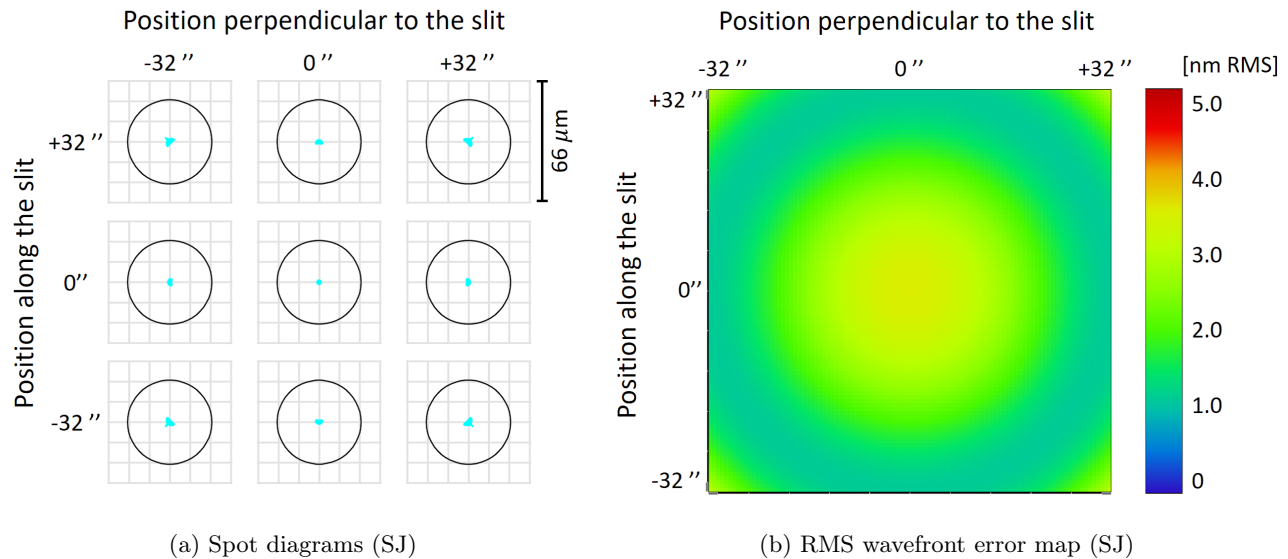(a) Spot diagrams (SJ)

(b) RMS wavefront error map (SJ)

Figure 8: Image qualities of the SCIP-SJ optical system. (a) Spot diagrams in the SCIP-SJ FOV. The horizontal direction shows the position perpendicular to the slit and the vertical direction shows the position along the slit. The black circle in the center represents an airy disk corresponding to F/24.2. The size of the box is 66 μm (equivalent to 6 pixels), which corresponds to 0.56 arcsecond. (b) RMS wavefront error map in the SCIP-SJ FOV.

5.2 SCIP-SJ Tolerance analysis and error budget plan

As with the SCIP-SP, we conducted tolerance analyses of SCIP-SJ to evaluate the performance, including assembly and manufacturing errors, to determine the number and stoke of the compensators. Based on the sensitivity and Monte Carlo analysis results with the feasible tolerance, we determined the needed compensators and alignment plan as follows:

(1) adjust the x-and y-tilt of the reflective notch filter and defocus of the detector to compensate for the image quality,

(2) adjust the x- and y-shift of the detector to compensate for the shift of the image position.

We revised the tolerance values to more feasible values and performed a Monte Carlo analysis under this alignment plan. The tolerance table of SJ are shown in Fig. 6b and the results of a Monte Carlo analysis assuming parabolic tolerance distributions (N = 1000) are shown in Fig. 9a. The RMS wavefront error at cumulative probability (3σ) is 19.1 nm RMS, which indicates that the wavefront error degradation due to installation and manufacturing error is 18.8 nm RMS by subtraction using root sum squares (RSS) approach. The error budget plan for imaging performance is also shown in Fig. 9b. Here, we assume that the surface figure errors, transmitted wavefront errors, and the adjustment errors are set to feasible values. The total RSS value is 33.2 nm RMS, which satisfies the requirements (34 nm RMS). The results of the error assessment due to environmental changes (temperature, humidity, and gravity direction) are also reported in Ref. 14
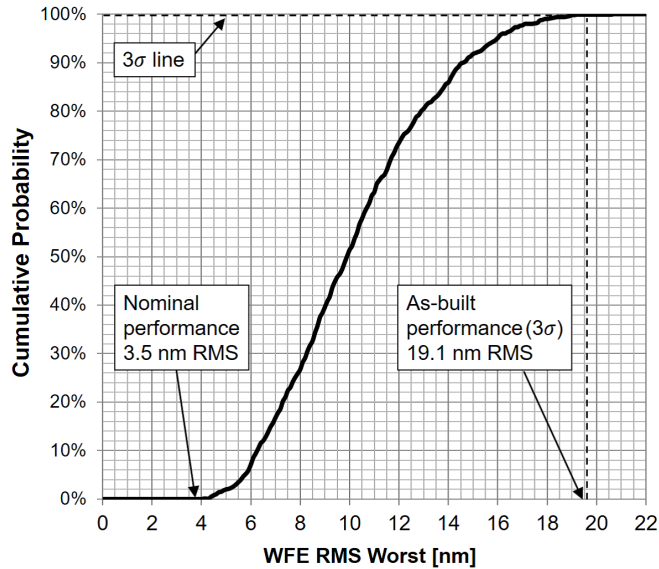
(a) Monte Carlo analysis result (SJ)

Error factor		RMS wavefront error [nm]
Nominal performance		3.5
Surface figure error	due to manufacturing	23.3
	due to mounting	12.7
Installation error (3σ) including manufacturing error		18.8
Adjustment error of compensators		3.4
Environmental change (temperature, humidity and gravity direction)		5.0
Root sum square		33.2

(b) RMS wavefront error budget plan (SJ)

Figure 9: Monte Carlo analysis results and an error budget plan for RMS wavefront error. (a) Monte Carlo analysis results. The Monte Carlo simulation is performed on 1,000 trials. We assumed a parabolic distribution, and an adjustment using three compensators. (b) RMS wavefront error budget plan.

6. STRAY LIGHT CONTROL AND ANALYSIS

To control unintended reflections and stray light in the SCIP optical system, we designed light traps and baffles as follows:

(1) Entrance baffle
To suppress unexpected scattered light from ISLiD.

(2) SJ optics box
To dump unwanted out-of-band light from slit transmitted by the reflective notch coating which has much larger energy compared to the reflected light and to suppress both unexpected scattered light from ISLiD.

(3) SJ camera baffle (attached to the SJ camera mount)
To prevent light at unexpected angle from entering the SJ sensor and suppress reflected light from it.

(4) Slit diffraction stop
To limit diffraction light from the slit and suppress unexpected scattered light from ISLiD.

(5) 0th order light stop
To stop 0th and unwanted orders of light from the grating and to suppress unexpected scattered light from ISLiD.

(6) Higher order light stop
To stop unwanted orders of light from the grating and work as a camera baffle for SP.

(7) PBS mask (attached to the PBS holder)
To stop the out-of-band light of SP coming to the PBS of each channel.

(8) SP camera baffle
To suppress unexpected light from SCIP .

The positions of these light traps and baffles are shown in Fig. 10. We conducted stray light analysis on a commercially available ray-trace-based analysis software (LightTools). The surface characteristics were based on
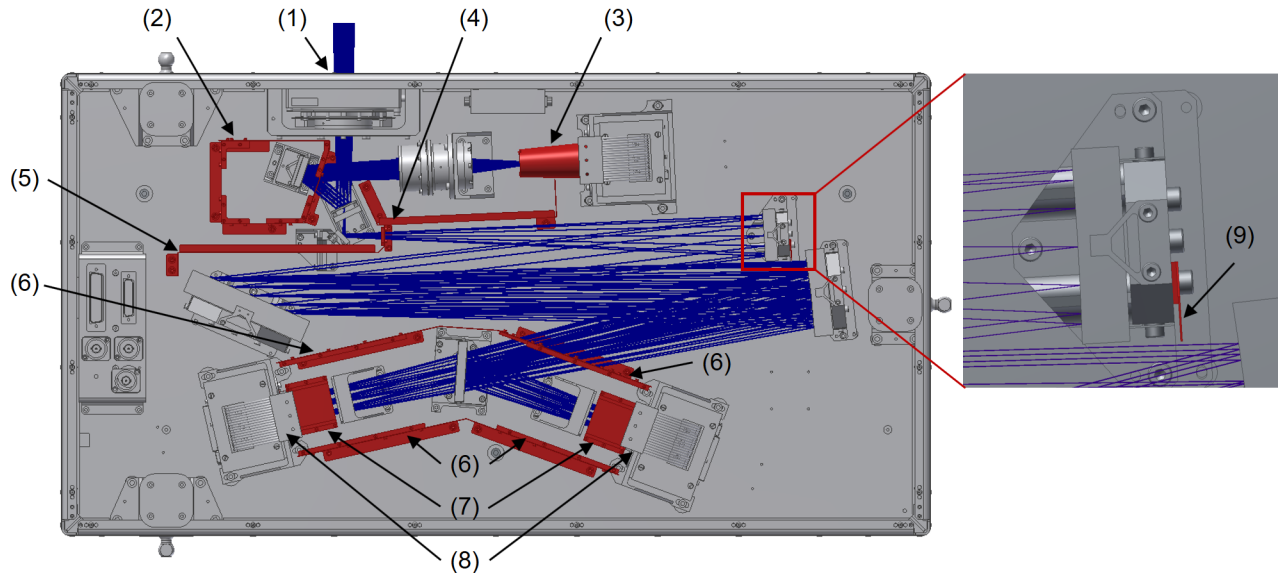
Figure 10: Structural model of SCIP. The blue lines represent the light paths of design and the red structures represent light traps and baffles. Note that the cover and the roofs of the boxes are not shown in this figure. (1) Entrance baffle, (2) SJ optics box, (3) SJ camera baffle, (4) Slit diffraction stop, (5) 0th order light stop, (6) Higher order light stop, (7) PBS mask, (8) SP camera baffle, and (9) SP collimator mirror baffle.

spectroscopic data measured by a spectrophotometer. Since the scattering distribution could not be measured, we performed an analysis assuming specular and Lambert scattering, and recorded the worse result. In order to accurately represent the echelle grating properties in LightTools, the grating properties of the echelle grating were calculated with a commercially available electromagnetic field analysis software (RSOFT), and the results in BSDF (bi-directional scattering distribution function) format were imported into LightTools. An example of BSDF data calculated by RSOFT is shown in Fig. 11. The correlation between the peak wavelength and the diffraction order was the same as that predicted by theory.
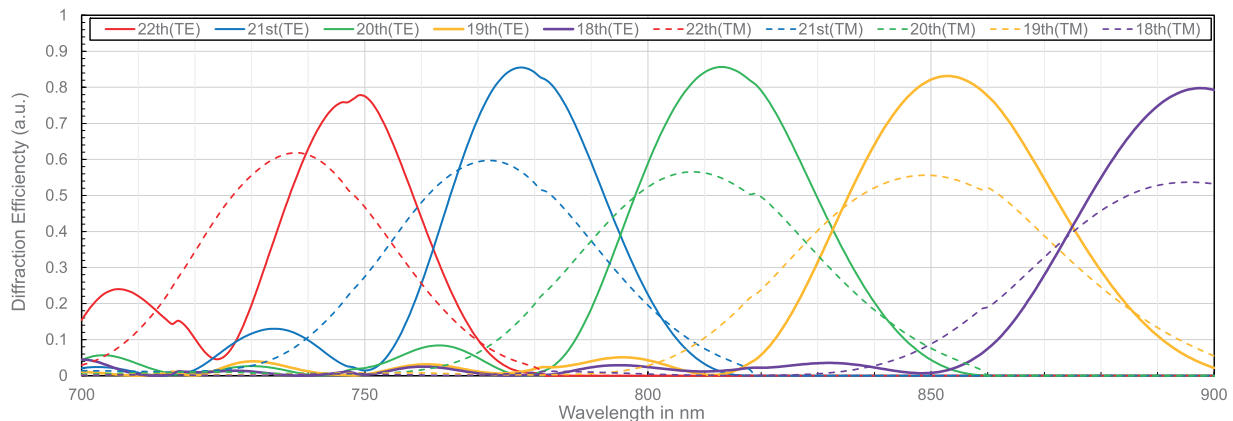

Figure 11: An example of BSDF data calculated by RSOFT. The results shown in this graph are for the incident angle relative to the grating normal of $63°$.

The results of the stray light analysis of the SCIP-SP optical system are shown in Fig. 12. The results indicate that the amount of stray light compared to the signal is up to approximately 2 % in irradiance. The main cause of the stray light was the multiple reflections on both sides of the slit. Based on this result, the backside of the

slit was masked with a blacken coating except for the part of the slit where the light transmits without a single reflection. This not only prevents multiple reflections inside the slit, but also prevents the effects of pinholes caused by manufacturing errors on the slit's front surface. We also found that the ghost image was caused by the paths reflected by the blocking filter and hitting the side and back surface of the collimator mirror. For this ghost, a new light trap was installed behind the collimator mirror. Stray light analysis of SJ showed that the main cause of stray light is the multiple reflection between the ND filter and the bandpass filter of light outside the SJ wavelength band. Stray light analysis of the SCIP-SJ shows that multiple reflections outside the band wavelengths between the ND filter and the bandpass filter are dominant in the SJ. Based on the results, we tightened the out-of-band transmission specification of the bandpass filter.
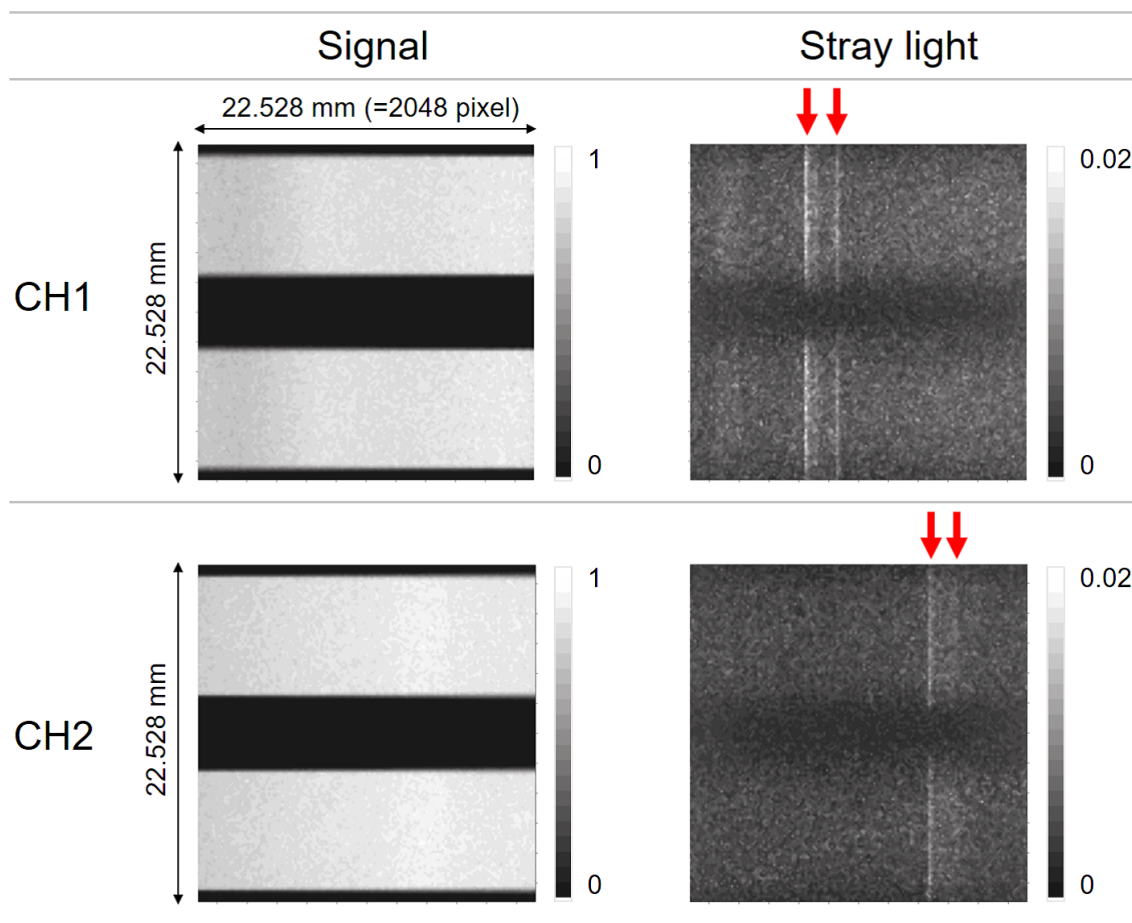

Figure 12: Results of the SCIP-SP stray light analysis. The left maps show the irradiance distributions of the science path and the right maps show those of the stray light. The amount of stray light to the signal was approximately 2 % in irradiance. The red arrows indicate the ghosts that hit the side of the collimator mirror.

7. SUMMARY

The SCIP optical system was designed to achieve high spatial and spectral resolutions, simultaneous observation at two wavelengths polarizations. SCIP-SP uses high-order aspherical mirrors, multiple orders of an echelle grating, a wedged beam splitter, and polarized beam splitters. Together with the SCIP-SJ optical system of doublet lenses and some filters, the optical system fits suitably in the limited space available. Alignment and error budget plans based on tolerance analysis are established and demonstrated the feasibility of this solution. To control unintended reflection and stray light in the SCIP optical system, some light traps and baffles are designed, and stray light analysis is performed to identify the main causes of stray light.

ACKNOWLEDGMENTS

REFERENCES

[1] Solanki, S. K., Barthol, P., Danilovic, S., Feller, A., Gandorfer, A., Hirzberger, J., Riethmüller, T. L., Schüssler, M., Bonet, J. A., Martínez Pillet, V., del Toro Iniesta, J. C., Domingo, V., Palacios, J., Knölker, M., Bello González, N., Berkefeld, T., Franz, M., Schmidt, W., and Title, A. M., "SUNRISE: Instrument, Mission, Data, and First Results," *Astrophys. J. Lett.* **723**, L127–L133 (Nov. 2010).

[2] Suematsu, Y., Katsukawa, Y., Hara, H., Ichimoto, K., Shimizu, T., Kubo, M., Barthol, P., Riethmueller, T., Gandorfer, A., Feller, A., Orozco Suárez, D., Del Toro Iniesta, J. C., Kano, R., Ishikawa, S.-n., Ishikawa, R., Tsuzuki, T., Uraguchi, F., Quintero Noda, C., Tamura, T., Oba, T., Kawabata, Y., Nagata, S., Anan, T., Cobos Carrascosa, J. P., Lopez Jimenez, A. C., Balaguer Jimenez, M., and Solanki, S., "Sunrise Chromospheric Infrared spectroPolarimeter (SCIP) for the SUNRISE balloon-borne solar observatory," in [*42nd COSPAR Scientific Assembly*], **42**, PSB.1–29–18 (July 2018).

[3] Katsukawa, Y., del Toro Iniesta, J. C., Solanki, S. K., Kubo, M., Hara, H., Shimizu, T., Oba, T., Kawabata, Y., Tsuzuki, T., Uraguchi, F., Nodomi, Y., Shinoda, K., Tamura, T., Suematsu, Y., Ishikawa, R., Kano, R., Ichimoto, K., Nagata, S., Noda, C. Q., Anan, T., et al., "Sᴜɴʀɪsᴇ Chromospheric Infrared spectroPolarimeter (SCIP) for Sᴜɴʀɪsᴇ III: System Design and Capability," *Ground-based and Airborne Instrumentation for Astronomy VIII, SPIE Astronomical Telescopes Instrumentation* **11447** (Dec. 2020).

[4] Tsuneta, S., Ichimoto, K., Katsukawa, Y., Nagata, S., Otsubo, M., Shimizu, T., Suematsu, Y., Nakagiri, M., Noguchi, M., Tarbell, T., Title, A., Shine, R., Rosenberg, W., Hoffmann, C., Jurcevich, B., Kushner, G., Levay, M., Lites, B., Elmore, D., Matsushita, T., Kawaguchi, N., Saito, H., Mikami, I., Hill, L. D., and Owens, J. K., "The Solar Optical Telescope for the Hinode Mission: An Overview," *Solar Physics* **249**, 167–196 (June 2008).

[5] Quintero Noda, C., Kato, Y., Katsukawa, Y., Oba, T., de la Cruz Rodríguez, J., Carlsson, M., Shimizu, T., Orozco Suárez, D., Ruiz Cobo, B., Kubo, M., et al., "Chromospheric polarimetry through multiline observations of the 850-nm spectral region–ii. a magnetic flux tube scenario," *Monthly Notices of the Royal Astronomical Society* **472**(1), 727–737 (2017).

[6] Quintero Noda, C., Villanueva, G. L., Katsukawa, Y., Solanki, S. K., Orozco Suárez, D., Ruiz Cobo, B., Shimizu, T., Oba, T., Kubo, M., Anan, T., Ichimoto, K., and Suematsu, Y., "Solar polarimetry in the K I D$_2$ line : A novel possibility for a stratospheric balloon," *Astronomy & Astrophysics* **610**, A79 (Mar. 2018).

[7] Nelson, P. G., Casini, R., de Wijn, A. G., and Knoelker, M., "The Visible Spectro-Polarimeter (ViSP) for the Advanced Technology Solar Telescope," *Ground-based and Airborne Instrumentation for Astronomy III, SPIE Astronomical Telescopes + Instrumentation* **7735**, 77358C (July 2010).

[8] Tritschler, A., Rimmele, T. R., Berukoff, S., Casini, R., Kuhn, J. R., Lin, H., Rast, M. P., McMullin, J. P., Schmidt, W., Wöger, F., and DKIST Team, "Daniel K. Inouye Solar Telescope: High-resolution observing of the dynamic Sun," *Astronomische Nachrichten* **337**, 1064 (Nov. 2016).

[9] Lites, B. W., Akin, D. L., Card, G., Cruz, T., Duncan, D. W., Edwards, C. G., Elmore, D. F., Hoffmann, C., Katsukawa, Y., Katz, N., Kubo, M., Ichimoto, K., Shimizu, T., Shine, R. A., Streand er, K. V., Suematsu, A., Tarbell, T. D., Title, A. M., and Tsuneta, S., "The Hinode Spectro-Polarimeter," *Solar Physics* **283**, 579–599 (Apr. 2013).

[10] Barthol, P., Gandorfer, A., Solanki, S. K., Schüssler, M., Chares, B., Curdt, W., Deutsch, W., Feller, A., Germerott, D., Grauf, B., Heerlein, K., Hirzberger, J., Kolleck, M., Meller, R., Müller, R., Riethmüller, T. L., Tomasch, G., Knölker, M., Lites, B. W., Card, G., Elmore, D., Fox, J., Lecinski, A., Nelson, P., Summers, R., Watt, A., Martínez Pillet, V., Bonet, J. A., Schmidt, W., Berkefeld, T., Title, A. M., Domingo, V., Gasent Blesa, J. L., Del Toro Iniesta, J. C., López Jiménez, A., Álvarez-Herrero, A., Sabau-Graziati, L., Widani, C., Haberler, P., Härtel, K., Kampf, D., Levin, T., Pérez Grand e, I., Sanz-Andrés, A., and Schmidt, E., "The Sunrise Mission," *Solar Physics* **268**, 1–34 (Jan. 2011).

[11] Berkefeld, T., Schmidt, W., Soltau, D., Bell, A., Doerr, H. P., Feger, B., Friedlein, R., Gerber, K., Heidecke, F., Kentischer, T., v. D. Lühe, O., Sigwarth, M., Wälde, E., Barthol, P., Deutsch, W., Gandorfer, A., Germerott, D., Grauf, B., Meller, R., Álvarez-Herrero, A., Knölker, M., Martínez Pillet, V., Solanki, S. K., and Title, A. M., "The Wave-Front Correction System for the Sunrise Balloon-Borne Solar Observatory," *Solar Physics* **268**, 103–123 (Jan. 2011).

[12] Gandorfer, A., Grauf, B., Barthol, P., Riethmüller, T. L., Solanki, S. K., Chares, B., Deutsch, W., Ebert, S., Feller, A., Germerott, D., Heerlein, K., Heinrichs, J., Hirche, D., Hirzberger, J., Kolleck, M., Meller, R., Müller, R., Schäfer, R., Tomasch, G., Knölker, M., Martínez Pillet, V., Bonet, J. A., Schmidt, W., Berkefeld, T., Feger, B., Heidecke, F., Soltau, D., Tischenberg, A., Fischer, A., Title, A., Anwand, H., and Schmidt, E., "The Filter Imager SuFI and the Image Stabilization and Light Distribution System ISLiD of the Sunrise Balloon-Borne Observatory: Instrument Description," *Solar Physics* **268**, 35–55 (Jan. 2011).

[13] Czerny, M. and Turner, A., "Über den astigmatismus bei spiegelspektrometern," *Zeitschrift für Physik* **61**(11-12), 792–797 (1930).

[14] Uraguchi, F., Tsuzuki, T., Katsukawa, Y., Hara, H., Iwamura, S., Kubo, M., Nodomi, Y., Suematsu, Y., Kawabata, Y., Shimizu, T., Solanki, S., and del Toro Iniesta, J. C., "Sunrise Chromospheric Infrared spectroPolarimeter (SCIP) for Sunrise III: Opto-mechanical analysis and design," *Ground-based and Airborne Instrumentation for Astronomy VIII, SPIE Astronomical Telescopes + Instrumentation* **11447** (Dec. 2020).